Applied Ocean Research 161 (2025) 104695

Contents lists available at ScienceDirect

Applied Ocean Research

journal homepage: www.elsevier.com/locate/apor

Multi-chamber cylindrical OWC: analytical model and numerical results

Antonino Simone Spanò [a,b], Giovanni Malara [a], Felice Arena [a,*]

[a] Natural Ocean Engineering Laboratory NOEL, "Mediterranea" University of Reggio Calabria, Via Zehender - Loc. Feo di Vito, 89122 Reggio Calabria, Italy
[b] University School of Advanced Studies, IUSS Pavia, Piazza della Vittoria 15, 27100 Pavia, Italy

ARTICLE INFO

Keywords:
Wave energy
Oscillating water column
Multi-chamber
Vertical cylinder
Analytical Solution
Eigenfunction Matching Method

ABSTRACT

Wave energy has the potential to play a crucial role in the ongoing energy transition towards the exploitation of renewable energy sources. Among the wave energy converters, Oscillating Water Column (OWC) is recognized to be one of the most promising technologies. Despite the amount of research conducted on those devices, there is no consensus on the optimal OWC configuration. In this context, circular OWCs emerged as an attractive option as it is a configuration unaffected by the direction of the incoming waves. Recently, research focused on devices equipped with multiple chambers in order to increase the overall device efficiency via the introduction of concentric chambers. This paper studies a multi-chamber concept arising from the partition of a cylindrical single chamber OWC into multiple chambers spanning a reduced inner angular width. Within the linearized potential flow theory, throughout the eigenfunction expansion matching method, and considering a linear power take off, a semi-analytical solution is obtained. Next, numerical results pertaining to the cases of a circular OWC comprising two and three chambers, spanning the whole inner sector, are discussed. The numerical analysis shows that the use of multiple chambers having a reduced angular width increases the overall energy-wise performance of the system with respect to the case of a single chamber OWC.

1. Introduction

The potential role of ocean energy in the transition from fossil fuel to renewable energy production is widely recognized (Cruz Joao, 2008; Mørk et al., 2010). In particular, estimates on the theoretical global wave energy potential stand upon 32 000 TWh/year (Lehmann et al., 2017; Taveira-Pinto et al., 2015), which is sufficient to meet the world energy demand of about 22,848 TWh/year reached in 2019 (IEA, 2021). Key characteristics of the wave energy resource are its predictability and its density distribution (about 2–3 kW/m^2), which is much higher than solar or wind energy densities, respectively, of 0.17 kW/m^2 and 0.5 kW/m^2 (Shi et al., 2024).

Various wave energy converters (WECs) have been proposed for harvesting the energy from sea waves. The classification of those devices made based on their working principle divides them into three categories: overtopping devices (ODs), oscillating bodies (OBs), oscillating water columns (OWCs) (Falcão, 2010). Among them, OWCs are the most promising in terms of reliability and energy production (Babarit, 2015). Their working principle is based on the oscillation of a water column induced by the wave motion through an opening located below the mean water level. This oscillation causes compression and decompression of the air pocket located above the water column, which in turn generates an alternating airflow through an opening at the top of the device. By using a turbine, this airflow can be harnessed to produce electrical energy. These devices can be deployed both offshore and onshore, either floating or fixed, and can be integrated into existing structures such as port harbors or breakwaters. The main geometrical configurations are rectangular and circular. In particular, the circular shape has the advantage of being unaffected by the direction of incoming waves.

Despite a relevant number of research projects has been conducted on those devices, there has not been reached convergence towards one type of design. Evans and Porter (1995) investigated the hydrodynamics within the linearized potential flow theory by considering a 2D thin vertical OWC. Martins-Rivas and Mei (2009) studied a circular OWC installed at the tip of a thin breakwater by showing, via an exact analytical solution, the independence of energy absorption from the direction of the incoming waves. Lovas et al. (2010) extended this analytical approach to examine a large circular OWC installed at the tip of a coastal corner for two specific geometries: a convex and a concave corner of right angle. By solving the radiation and diffraction problems via the eigenfunction expansion matching method, they demonstrated

* Corresponding author.
E-mail address: arena@unirc.it (F. Arena).

https://doi.org/10.1016/j.apor.2025.104695
Received 23 January 2025; Received in revised form 21 May 2025; Accepted 2 July 2025
Available online 11 July 2025

the effects of the main geometrical parameters. In order to enhance the wave energy production, Deng et al. (2014) developed an analytical theory for a circular bottom-mounted OWC equipped with a V-shaped channel at the opening. Michele et al. (2019) investigated a circular OWC provided with an internal cylinder and a skirt on the external cylinder and assessed its remarkable effects on the global OWC response. Zheng et al. (2020) studied the size and position of the chamber opening. All of the circular OWCs previously investigated consider an inner chamber spanning the whole circular sector. Instead, the parametric investigations conducted by Spanò et al. (2024) on a circular OWC, showed that reducing the angular width of the chamber is an effective strategy to improve the overall OWC energy performance.

Recently research focused on devices hosting multiple chambers to increase overall efficiency. Ning et al. (2018) improved the design proposed by Zhou et al. (2018) by introducing a concentric shell to investigate the surface elevation and energy conversion efficiency. The two chambers were connected at the top of the device. Results show the broadening of the operative frequency bandwidth. Gang et al. (2022) presented a cylindrical dual-chamber OWC semi-embedded into a breakwater and investigated the effects of the opening angle of the chamber. The effects of multiple chambers (up to 5 chambers) have been numerically and experimentally evaluated (Fu et al., 2023; Ning et al., 2024). The multi-chamber configurations show an increase in energy efficiency and frequency bandwidth. However, a large number of chambers does not yield a higher global efficiency, due to the wave induced interferences. A stationary cylindrical offshore OWC equipped with three concentric chambers was analytically investigated by Qian et al. (2024), by providing the effects of the number of chambers, and of the main geometrical parameters. The research carried out by Liu et al. (2024) experimentally evaluated a compact-ring OWC device called Rainbow using 1:10 scale fixed models in a wave tank. Two configurations (B-BDB and F-BDB) were tested under regular and irregular waves. Performance varied by module position and wave conditions. The F-BDB setup showed superior energy capture, reaching a peak capture width ratio of 0.26. Results provide benchmarks for future floating designs and optimizations.

This paper introduces a multi-chamber concept construed by partitioning a single cylindrical OWC with multiple chambers of reduced angular width, covering the same circular ring. The notable feature of this device is that the water column operates only in the vicinity of external cylindrical boundary. Therefore, it can be employed in conjunction with or totally embedded into complex systems or infrastructures, such as multi-purpose platforms or Very Large Floating Structures (Abhinav et al., 2020; Lamas-Pardo et al., 2015). This article develops a mathematical model based upon the linearized potential flow theory for quantifying the response and power output of this system under the assumption that it is equipped with a linear Power Take-Off (PTO) unit. Specifically, it analyses two case studies concerning a cylindrical OWC with two and three chambers spanning the whole circular sector. Also, a comparison between single and multi-chamber OWC outputs has been made in order to emphasize advantages and disadvantages of the proposed configuration. In passing, note that the mathematical model herein developed can be applied also to other geometrical configurations involving, for instance, a higher number of chambers or even the case of OWC chambers occupying only a limited portion of the cylindrical structure.

The paper is organized as follows. Section 2 describes the mathematical model. Section 3 shows the numerical results and the comparison between single and multi-chamber OWCs. Conclusions are given in Section 4.

2. Mathematical model

The investigated structure is a vertical floating cylinder (Fig. 1)

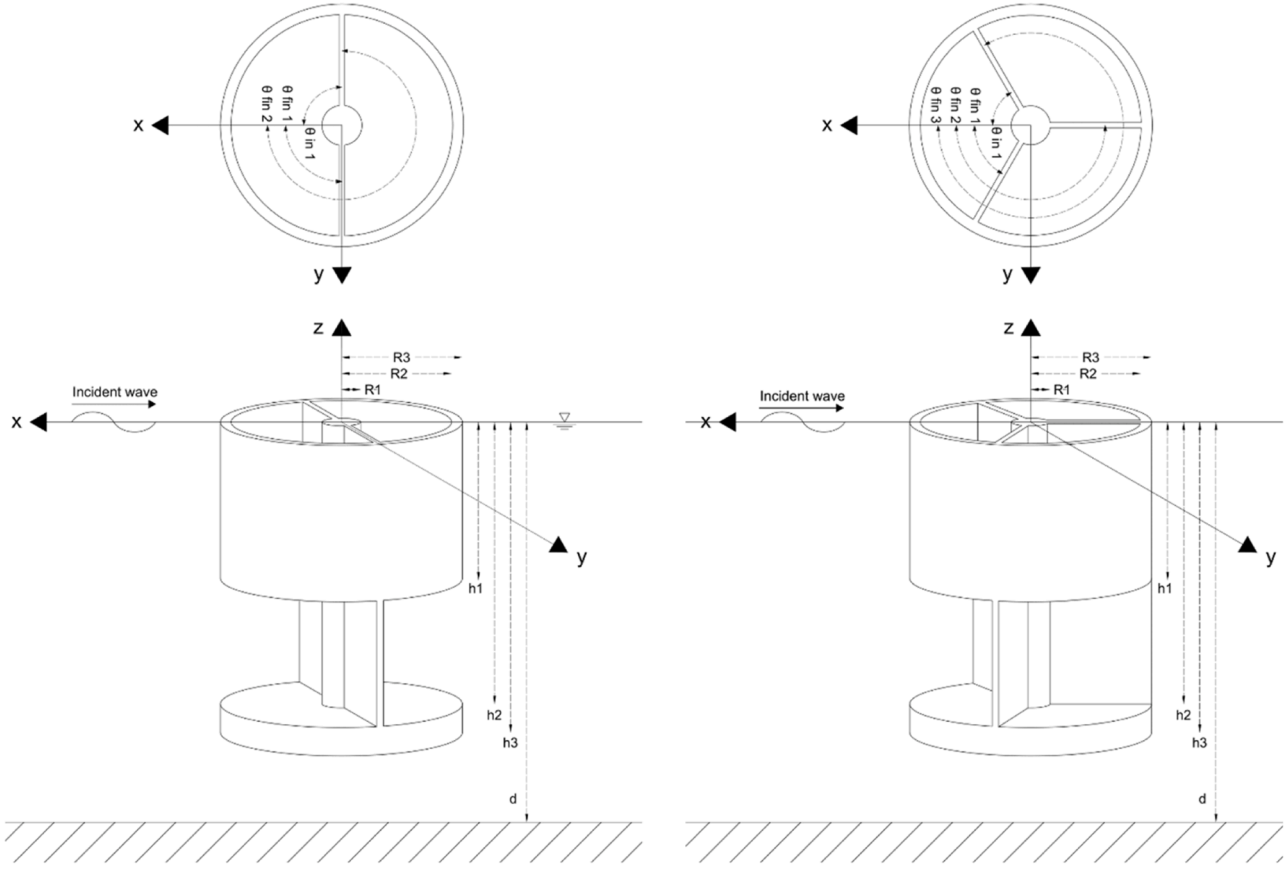

Fig. 1. Three-dimensional view (lower panels) and plan-view (upper panels) of the 2-chamber OWC (left panels) and of the 3-chamber OWC (right panels).

described in a cartesian coordinate system O_{xyz} with the origin located at the intersection of the mean water level (O_{xy} plane) and the vertical central axis of the cylinder. Considering a constant water depth d, the structure is submerged up to a depth h_3, and has opening between h_1 and h_2. The chamber is partitioned into N_c chambers, characterized by equal radial width $\Delta R = R_2 - R_1$ and angular amplitude $\Delta\theta_{nc} = \theta_{fin-nc} - \theta_{in-nc}$ (in which $n_c = 1, 2, \ldots, N_c$), It is important to note that, assuming that the inner walls separating the OWC chambers are infinitely small and by considering that all the chambers have the same angular width, $\theta_{in-nc} = \theta_{fin-(nc-1)}$ for $n_c > 1$. For mathematical convenience, the chambers are distributed such that the bisector of the first one is aligned with the x-axis, which is the axis of wave propagation.

The mathematical model is developed by adopting the linearized potential flow theory. Therefore, the fluid is assumed inviscid and incompressible, and the water particle motion is irrotational. The theory is employed by working in a cylindrical vertical coordinate system (r, θ, z) in which the z-axis is the axis of the vertical cylinder, and the origin of this cylindrical reference frame is located at the centre of the cylinder on the mean water level. In this context, the mathematical problem is formulated through the scalar velocity potential function:

$$\Phi(r, \theta, z,\ t) = Re\{\phi(r, \theta, z)\ e^{-i\omega t}\}, \tag{1}$$

where $Re\{\cdot\}$ denotes the real part of a complex number; i is the imaginary unit; ω is the angular wave frequency; and t is the time variable. Time dependence is sorted out by considering a time-harmonic motion.

The linearized potential flow theory allows applying the superposition principle, as done by Evans and Porter (1995). The potential is given by the superposition of three contributions: incident, diffracted, and radiated potentials.

$$\phi(r, \theta, z) = \phi_I(r, \theta, z) + \phi_D(r, \theta, z) + \sum_{j=1}^{N_c} \phi_{R,j}(r, \theta, z) \tag{2}$$

where $\phi_I(r, \theta, z)$ is the incident wave field, $\phi_D(r, \theta, z)$ is the diffracted wave field, $\phi_{R,j}$ are the radiated wave fields associated with the motion of each oscillating water column. The incident potential flow in cylindrical coordinates, as reported by Linton and McIver (2001), for an incident plane wave propagating from the positive x direction is

$$\phi_I(r, \theta, z) = -\frac{igA}{\omega}\ e^{k_0 r\cos\theta}\chi_0(z) = -\frac{igA}{\omega}\ \sum_{m=0}^{+\infty} \epsilon_m(-i^m)\cos(m\theta)\ J_m(kr)\frac{\chi_0(z)}{\chi_0(0)}, \tag{3}$$

in which A is the wave amplitude, $k_0 = -ik$ is the wavenumber, ϵ_m is the Neumann symbol (1 if $m = 0$; 2 if $m > 0$), $J_m(kr)$ is the Bessel function of the first kind of order m, and $\chi_0(z)$ is the vertical eigenfunction. The wave number is the solution of the equation

$$k_n \tan(k_n d) = -\frac{\omega^2}{g}, \tag{4}$$

in which $n = 0$ denotes the propagating mode, and k_n with $n > 0$ the evanescent modes. The vertical eigenfunction is given by the equation

$$\chi_0(z) = \cos[k_0(z+d)]\left\{\frac{1}{2}\left[1 + \frac{\sin(2k_0 d)}{2k_0 d}\right]\right\}^{-0.5}. \tag{5}$$

2.1. Boundary value problem

In order to describe the diffracted and radiated potentials, the domain is partitioned into $2 + 2N_c$ sub-domains:

$$\Omega_1(r,\ \theta,\ z) = \{\ \mathrm{r} \in [R_3;\ +\infty);\ z \in [-d;\ 0];\ \theta \in [0; 2\pi]\},$$

$$\Omega_2(r,\ \theta,\ z) = \{\mathrm{r} \in [0;\ R_3];\ z \in [-d;\ -h_3];\ \theta \in [0; 2\pi]\},$$

$$\Omega_{3-n_c}(r,\ \theta,\ z) = \left\{\mathrm{r} \in [\mathrm{R}_1;\ R_2];\ z \in [-h_2;\ 0];\ \theta \in \left[\theta_{\mathrm{in-nc}}; \theta_{\mathrm{fin-nc}}\right]\right\},\ \text{for } n_c = 1, \ldots, N_c$$

and

$$\Omega_{4-n_c}(r,\ \theta,\ z) = \left\{\mathrm{r} \in [\mathrm{R}_2;\ R_3];\ z \in [-h_2; -h_1];\ \theta \in \left[\theta_{\mathrm{in-nc}}; \theta_{\mathrm{fin-nc}}\right]\right\},\ \text{for } n_c = 1, \ldots, N_c.$$

Denoting $\phi_{\lambda,i}$ either diffracted ($\lambda = D$) or radiated ($\lambda = R$) potential into the i th subdomain, the following boundary value problem is posed:

$$\nabla^2\phi_{\lambda,i}\ (r,\ \theta,\ z) = 0 \tag{6}$$

$$\frac{\partial\phi_{\lambda,1}}{\partial z} - \frac{\omega^2}{g}\ \phi_{\lambda,1} = 0 \ at\ z = 0\ \text{in}\ \Omega_1 \tag{7}$$

$$\frac{\partial\phi_{\lambda,3-n_c}}{\partial z} - \frac{\omega^2}{g}\ \phi_{\lambda,3-n_c} = \begin{cases} 0,\ at\ z = 0\ in\ \Omega_{3-nc},\ \lambda = D \\ \dfrac{i\omega P_{n_c}}{\rho g}\ \delta_{r\ n_c},\ at\ z = 0\ in\ \Omega_{3-nc},\ \lambda = R \end{cases},\ \text{for } n_c = 1, \ldots, N_c \tag{8}$$

$$\frac{\partial\phi_{\lambda,i}}{\partial \boldsymbol{n}} = 0 \text{ on the structural solid boundary and on the seabed} \tag{9}$$

$$\lim_{kr\ \to\ \infty} \sqrt{r}\left(\frac{\partial\phi_{\lambda,1}}{\partial z} - ik\phi_{\lambda,1}\right) = 0 \tag{10}$$

In Eqs. (6–10) P_{n_c} is the air pressure amplitude inside the chamber n_c, ρ is the water density, $\boldsymbol{n}$ is the unit vector normal to the solid boundary, and $\delta_{r\ n_c}$ is the Kronecker delta function ($\delta_{n_c\ n_c} = 1$, otherwise $\delta_{r\ n_c} = 0$).

2.2. Velocity potentials

The solution to the boundary value problem (6–10) is sought by the eigenfunction expansion matching technique, which allows representing the velocity potentials into each subdomain as

$$\phi_{\lambda,\ 1} = \sum_{m=0}^{\infty}\sum_{n=0}^{\infty} \alpha_{mn}^{(\lambda,\ 1)} F_{mn}^{(1)}\ \cos(m\theta)\chi_n^{(1)}(z) + \phi_I\delta_{\lambda D}, \tag{11}$$

$$\phi_{\lambda,\ 2} = \sum_{m=0}^{\infty}\sum_{n=0}^{\infty} \alpha_{mn}^{(\lambda,\ 2)} F_{mn}^{(2)}\ \cos(m\theta)\chi_n^{(2)}(z), \tag{12}$$

$$\phi_{\lambda,\ 3-n_c} = \sum_{m=0}^{\infty}\sum_{n=0}^{\infty}\left[\alpha_{mn}^{(\lambda,\ 3A-n_c)}F_{mn}^{(3A-n_c)} + \alpha_{mn}^{(\lambda,\ 3B-n_c)}F_{mn}^{(3B-n_c)}\right]\cos\left[m\beta_{n_c}(\theta-\theta_{in-n_c})\right]\chi_n^{(3)}(z) + \delta_{\lambda R}, \tag{13}$$

and

$$\phi_{\lambda,\ 4-n_c} = \sum_{m=0}^{\infty}\sum_{n=0}^{\infty}\left[\alpha_{mn}^{(\lambda,\ 4A-n_c)}F_{mn}^{(4A-n_c)} + \alpha_{mn}^{(\lambda,\ 4B-n_c)}F_{mn}^{(4B-n_c)}\right]\cos\left[m\beta_{n_c}(\theta-\theta_{in-n_c})\right]\chi_n^{(4)}(z), \tag{14}$$

where $\delta_{\lambda S}$ ($\delta_{\lambda R}$) is the Kronecker delta function, which is used for representing both the diffracted velocity potential $\delta_{DD}=1$ and the radiated potential $\delta_{RR}=1$, otherwise $\delta_{RD}=\delta_{DR}=0$. The coefficient $\beta_{n_c}=\frac{\pi}{\Delta\theta_{n_c}}$; and $\alpha_{mn}^{(\lambda,\ 1)}$, $\alpha_{mn}^{(\lambda,\ 2)}$, $\alpha_{mn}^{(\lambda,\ 3A-n_c)}$, $\alpha_{mn}^{(\lambda,\ 3B-n_c)}$, $\alpha_{mn}^{(\lambda,\ 4A-n_c)}$, and $\alpha_{mn}^{(\lambda,\ 4B-n_c)}$ are unknown coefficients. The terms $F_{mn}^{(1)}$, $F_{mn}^{(2)}$, $F_{mn}^{(3A-n_c)}$, $F_{mn}^{(3B-n_c)}$, $F_{mn}^{(4A-n_c)}$, and $F_{mn}^{(4B-n_c)}$ are dependent on the Bessel functions. Specifically,

$$F_{mn}^{(1)} = \frac{K_m\left(k_n^{(1)}r\right)}{K_m\left(k_n^{(1)}R_3\right)}, \tag{15}$$

$$F_{mn}^{(2)} = \begin{cases} \left(\dfrac{r}{R_3}\right)^m & n=0 \\ \dfrac{I_m\left(k_n^{(2)}r\right)}{I_m\left(k_n^{(2)}R_3\right)} & n>0 \end{cases} \tag{16}$$

$$F_{mn}^{(3A-n_c)} = \frac{I_{m\beta_{n_c}}\left(k_n^{(3)}r\right)}{I_{m\beta_{n_c}}\left(k_n^{(3)}R_2\right)}, \tag{17}$$

$$F_{mn}^{(3B-n_c)} = \frac{K_{m\beta_{n_c}}\left(k_n^{(3)}r\right)}{I_{m\beta_{n_c}}\left(k_n^{(3)}R_2\right)}, \tag{18}$$

$$F_{mn}^{(4A-n_c)} = \begin{cases} \left(\dfrac{r}{R_3}\right)^m & n=0 \\ \dfrac{I_{m\beta_{n_c}}\left(k_n^{(4)}r\right)}{I_{m\beta_{n_c}}\left(k_n^{(4)}R_3\right)} & n>0 \end{cases} \tag{19}$$

$$F_{mn}^{(4B-n_c)}(r) = \begin{cases} \ln\left(\dfrac{r}{R_2}\right)+1 & n=m=0 \\ \left(\dfrac{r}{R_2}\right)^{-m} & n=0;\ m>0 \\ \dfrac{K_{m\beta_{n_c}}\left(k_n^{(4)}r\right)}{K_{m\beta_{n_c}}\left(k_n^{(4)}R_2\right)} & n>0; m>0 \end{cases} \tag{20}$$

being I_m and K_m ($I_{m\beta_{n_c}}$ and $K_{m\beta_{n_c}}$) the modified Bessel functions of order m (or $m\beta_{n_c}$) (Abramowitz and Stegun, 1964). Each subdomain is characterized by wavenumber $k_n^{(i)}$, and vertical eigenfunction $\chi_n^{(i)}$ such that,

$$k_n^{(1)}\tan\left(k_n^{(1)}d\right) = -\frac{\omega^2}{g}, \tag{21}$$

$$k_n^{(2)} = \frac{n\pi}{d-h_3} \tag{22}$$

$$k_n^{(3)}\tan\left(k_n^{(3)}h_2\right) = -\frac{\omega^2}{g} \tag{23}$$

$$k_n^{(4)} = \frac{n\pi}{h_2-h_1} \tag{24}$$

$$\chi_n^{(1)}(z) = \cos\left[k_n^{(1)}(z+d)\right]\left\{\frac{1}{2}\left[1+\frac{\sin\left(2k_n^{(1)}d\right)}{2k_n^{(1)}d}\right]\right\}^{-0.5} \tag{25}$$

$$\chi_n^{(2)}(z) = \begin{cases} \cos\left[k_0^{(2)}\ (z+d)\right],\ for\ n=0 \\ (1/2)^{-0.5}\cos\left[k_n^{(2)}\ (z+d)\right],\ for\ n>0 \end{cases} \tag{26}$$

$$\chi_n^{(3)}(z) = \cos\left[k_n^{(3)}(z+h_2)\right]\left\{\frac{1}{2}\left[1+\frac{\sin\left(2k_n^{(3)}h_2\right)}{2k_n^{(3)}h_2}\right]\right\}^{-0.5} \tag{27}$$

and

$$\chi_n^{(4)}(z) = \begin{cases} \cos\left[k_0^{(4)}\ (z+h_2)\right],\ for\ n=0 \\ (1/2)^{-0.5}\cos\left[k_n^{(4)}\ (z+h_2)\right],\ for\ n>0 \end{cases} \tag{28}$$

2.3. Computation of the unknown coefficients

To obtain the unknown coefficients $\alpha_{mn}^{(\lambda,\ 1)}$, $\alpha_{mn}^{(\lambda,\ 2)}$, $\alpha_{mn}^{(\lambda,\ 3A-n_c)}$, $\alpha_{mn}^{(\lambda,\ 3B-n_c)}$, $\alpha_{mn}^{(\lambda,\ 4A-n_c)}$, and $\alpha_{mn}^{(\lambda,\ 4B-n_c)}$, the continuity of pressure and horizontal velocity across two adjacent boundaries of two contiguous subdomains is enforced. That is,

$$\left(\phi_{\lambda,\ 1}\right)_{r=R_3} = \left(\phi_{\lambda,\ 2}\right)_{r=R_3}\ z\in[-d;\ -h_3];\ \theta\in[0;2\pi] \tag{29}$$

$$\left(\phi_{\lambda,\ 1}\right)_{r=R_3} = \left(\phi_{\lambda,\ 4-n_c}\right)_{r=R_3}\ z\in[-h_2;\ -h_1];\ \theta\in\left[\theta_{\text{in}-\text{nc}};\theta_{\text{fin}-\text{nc}}\right] \tag{30}$$

$$\left(\phi_{\lambda,\ 3-n_c}\right)_{r=R_2} = \left(\phi_{\lambda,4-n_c}\right)_{r=R_2}\ z\in[-h_2;\ -h_1];\ \theta\in\left[\theta_{\text{in}-\text{nc}};\theta_{\text{fin}-\text{nc}}\right] \tag{31}$$

$$\left(\frac{\partial\phi_{\lambda,\,1}}{\partial r}\right)_{r=R_3} = \begin{cases} 0,\ z\in[-h_1;0\,];\ \theta\in[0;2\pi] \\ \left(\frac{\partial\phi_{\lambda,\,4-n_c}}{\partial r}\right)_{r=R_3},\ z\in[-h_2;-h_1\,];\ \theta\in\left[\theta_{\text{in}-\text{nc}};\theta_{\text{fin}-\text{nc}}\right] \\ \left(\frac{d\partial\phi_{\lambda,\,2}}{\partial dr}\right)_{r=R_3},\ z\in[-d;\ -h_3];\ \theta\in[0;2\pi] \end{cases} \tag{32}$$

$$\left(\frac{\partial\phi_{\lambda,\,3-n_c}}{\partial r}\right)_{r=R_2} = \begin{cases} 0,\ z\in[-h_1;\,0];\ \theta\in\left[\theta_{\text{in}-\text{nc}};\theta_{\text{fin}-\text{nc}}\right] \\ \left(\frac{\partial\phi_{\lambda,\,4-n_c}}{\partial r}\right)_{r=R_2},\ z\in[-h_2;\ -h_1];\ \theta\in\left[\theta_{\text{in}-\text{nc}};\theta_{\text{fin}-\text{nc}}\right] \end{cases} \tag{33}$$

The coefficients are determined by projecting Eqs. (29)-(33) in the space of vertical eigenfunctions, where the unknown coefficients are calculated as the solution of a linear system of algebraic equations obtained by truncating the infinite series expansions.

2.4. PTO system

The power output of each OWC is computed under the assumption that the air pressure is uniform inside the chambers. For this purpose, the volume flow rate into each air chamber is computed by the equation

$$q_{n_c}(t) = q_{R-n_c}(t) + q_{E-n_c}(t),\ \text{for } n_c = 1,\ldots,N_c \tag{34}$$

so that the volume flow is given by the superposition of the radiation flow rate (generated by the air pressure fluctuations into the chambers), and the excitation flow rate (generated by the incident and diffracted wave fields). Following the approach presented by Falcão et al. (2016), a linear relationship between the volume flow rate and the air pressure inside the chamber is considered:

$$q_{n_c}(t) = \frac{V_{0,n_c}}{\nu\, p_{\text{atm}}}\frac{dp_{n_c}}{dt} + C_{PTO,n_c}p_{n_c}(t),\ \text{for } n_c = 1,\ldots,N_c \tag{35}$$

that takes into account the volume of air inside the chamber V_{0,n_c} in still conditions, the polytropic term ν related to the average efficiency of the turbine (necessary to express the relationship between the fluctuation of air density inside and outside the chamber), the air chamber pressure $p_{n_c}(t)$, and the turbine characteristics C_{PTO,n_c} (in terms of diameter and rotational speed).

Considering the linearity of eq. (35) and the time dependence in the velocity potential (1), flow rates and pressures can be analysed in frequency domain. That is,

$$\left\{q_{nc}(t),\ q_{E-n_c}(t),\ q_{R-n_c}(t),\ p_{n_c}(t)\right\} = \left\{Q_{n_c},\ Q_{E-n_c},\ Q_{R-n_c},\ \mathrm{P}_{n_c}\right\}e^{-i\omega t},\ \text{for } n_c = 1,\ldots,N_c \tag{36}$$

The excitation volume flow rates can be regarded as the elements of a vector Q_E, that are computed directly from the diffracted potentials by the equation

$$\{\boldsymbol{Q}_E\}_{n_c} = \int_{-\frac{\Delta\theta_{n_c}}{2}}^{+\frac{\Delta\theta_{n_c}}{2}}\int_{R_1}^{R_2}\left(\frac{\partial\phi_{D,3-n_c}}{\partial z}\right)_{z=0} rdrd\theta \tag{37}$$

Similarly, the radiated flow rates can be computed by defining a matrix Q_R having dimension $N_c \times N_c$, whose elements are given by the equation,

$$\{Q_R\}_{n_c j} = \{P\}_j \int_{-\frac{\Delta\theta_{n_c}}{2}}^{+\frac{\Delta\theta_{n_c}}{2}}\int_{R_1}^{R_2}\left(\frac{\partial\phi_{R,3-n_c}}{\partial z}\right)_{z=0} rdrd\theta = -\left(\{C\}_{n_c j} - i\{M_{ADD}\}_{n_c j}\right)\{P\}_j, \tag{38}$$

Table 1
OWC geometrical parameters.

d	10 m
R_1/d	0.1
R_2/d	0.5
R_3/d	0.55
h_1/d	0.2
h_2/d	0.6
h_3/d	0.65

where P is a vector encapsulating the chamber's air pressure amplitudes, and C and M_{ADD} are radiation damping and added mass matrices, respectively. It is worthy to note that the diagonal elements of the matrix having dimensions $[N_c \times N_c]$ represent the values produced by the radiation activated in the chamber under consideration, while the off-diagonal terms indicate the values observed in adjacent chambers due to radiation from the considered chamber.

From Eqs. (34) and (35), using the formulation of Eqs. (37) and (38), the relationship providing the air pressure amplitudes is derived. That is,

$$P = \left[C_{PTO} + C - i(M_{PTO} + M_{ADD})\right]^{-1}Q_E, \tag{39}$$

in which M_{PTO} and C_{PTO} are diagonal matrices with non-zero diagonal elements given by the equations

$$\{M_{PTO}\}_{n_c n_c} = \frac{\omega V_{0,n_c}}{\nu p_{atm}}, \tag{40}$$

and

$$\{\mathrm{C}_{\mathrm{PTO}}\}_{n_c n_c} = \sqrt{\{C\}_{n_c n_c}{}^2 + \left(\{M_{PTO}\}_{n_c n_c} + \{M_{ADD}\}_{n_c n_c}\right)^2}. \tag{41}$$

In this regard, note that $\mathrm{C}_{\mathrm{PTO}}$ is derived under the stipulation that the power absorption is optimal (Michele et al., 2019). Given the air pressure amplitudes, the mean power available to the turbine is readily calculated by the equation,

$$P_{m,n_c} = \frac{1}{2}\{C_{PTO}\}_{n_c n_c}|\{P\}_{n_c}|^2. \tag{42}$$

In order to evaluate the energy performances of the device, the capture width (Babarit, 2015) $CW_{n_c}(\Delta\theta)$ pertaining to the chamber n_c having angular width $\Delta\theta_{n_c}$ is employed. It is defined as the ratio between the mean power available at the turbine and the incident wave power:

$$CW_{n_c}(\Delta\theta_{n_c}) = \frac{P_{m,n_c}}{P_{in}}. \tag{43}$$

The incident wave power is calculated by the equation

$$P_{in} = \frac{1}{2}\rho g C_g A^2, \tag{44}$$

C_g being the wave group celerity and A being the incident wave amplitude.

3. Numerical results

Herein, a description of the OWC geometrical configuration utilized for estimating the power output of the system is presented in conjunction with numerical studies assessing the convergence of the proposed velocity potential representations. Next, the numerical results pertaining to the case of multi-chamber OWCs comprising $N_c = 2$ and $N_c = 3$ chambers are discussed. In all case studies, the air chamber height is z_c=10 m. The main geometrical parameters of the OWC configuration are shown in Table 1.

Prior to the determination of the OWC response, a numerical study has been conducted to evaluate the convergence of the developed eigenfunction expansion. Considering the case of an OWC with $N_c = 2$, Fig. 2 shows the results in terms of volume excitation flow rate, radiation

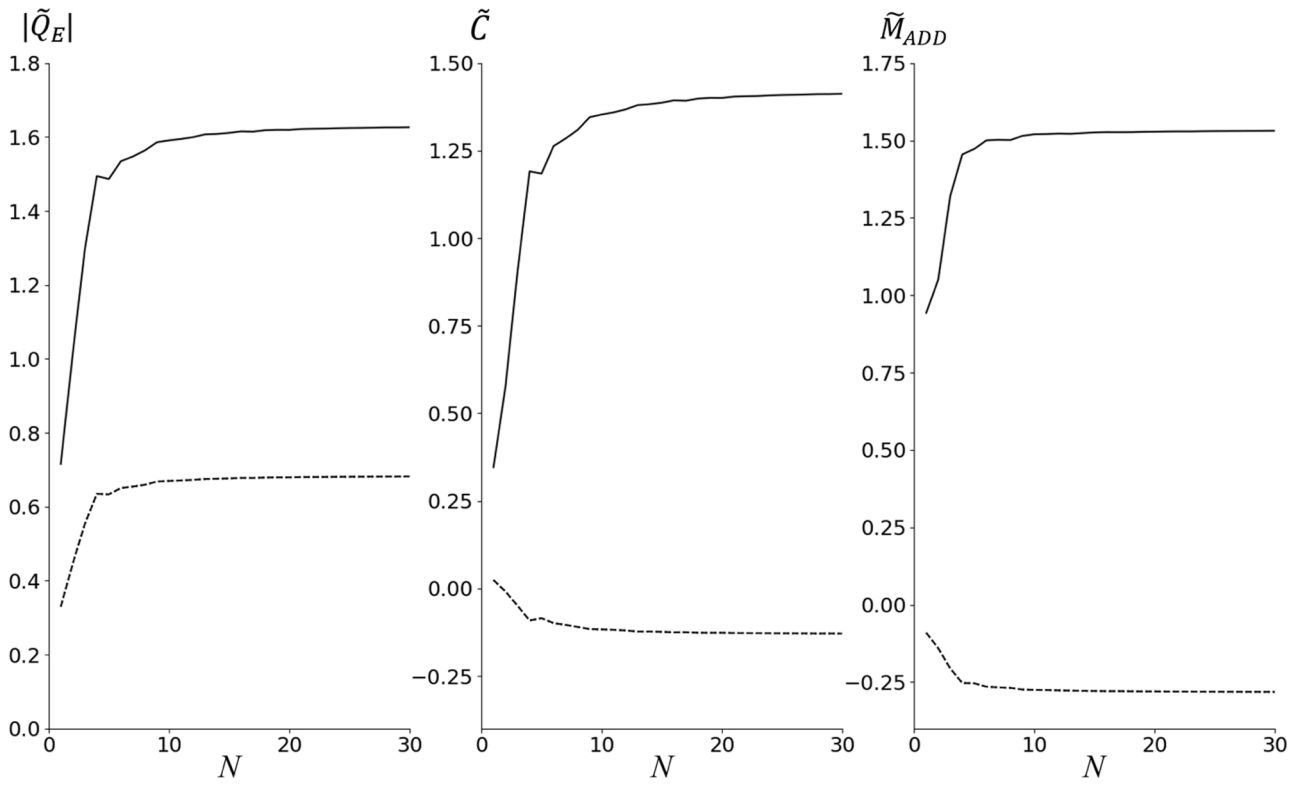

Fig. 2. Convergence study for a fixed geometry and frequency =1.35, in terms of Volume excitation flow, Radiation damping, Added mass (Continuous line: frontal chamber, dashed line: backside chamber).

damping and added mass into the up-wave and down-wave chambers. All of them are normalized as proposed by Lovas et al. (2010):

$$\widetilde{Q}_E = \frac{\sqrt{g/d}}{A\, d\, g}\, Q_E;\ (\widetilde{C},\ \widetilde{M}_{ADD}) = \frac{\rho\sqrt{g/d}}{d}\, (C,\ M_{ADD}). \tag{45}$$

In passing, note that the plots show the frequency domain behaviour of the diagonal elements $\{C\}_{1,1}$ and $\{M_{ADD}\}_{1,1}$, and of the off-diagonal elements $\{C\}_{1,2}$ and $\{M_{ADD}\}_{1,2}$. These elements are sufficient to characterize the entire added mass and radiation damping matrices, as the geometrical configuration of the investigated OWC implies that these are Toeplitz matrices (Gray, 2006).

The numerical results show that convergence to reliable estimates is obtained by retaining $N = 20$ and $M = 10$ terms.

The next subsections show also the free surface elevation inside the chambers evaluated as

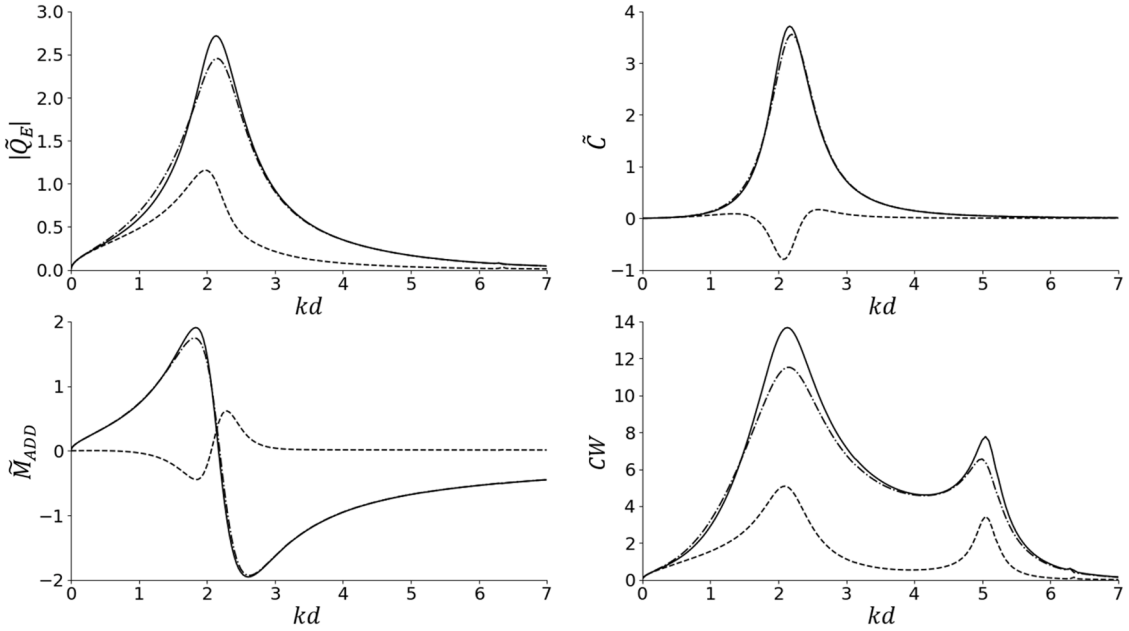

Fig. 3. Double chamber OWC (Continuous lines: upwave chamber; dashed lines: downwave chamber; dashed-dotted lines: single upwave chamber).

$$\eta(r,\theta) = Re\left\{A\phi_D(r,\theta,0) + \frac{1}{\rho g}\sum_{j=1}^{N_c}\{\boldsymbol{P}\}_j\phi_{Rj}(r,\theta,0)\right\}, \tag{46}$$

where an incident wave of unitary amplitude has been considered ($A = 1$).

To assess the advantages and disadvantages of a multi-chamber system, the $q_{factor}(\Delta\theta)$ and the $r_{factor}(\Delta\theta)$ are used. They are given by the equations

$$q_{factor}(\Delta\theta) = \frac{\sum_{n_c=1}^{N_c} CW_{n_c}(\Delta\theta)}{N_c CW(\Delta\theta)}, \tag{47}$$

and

$$r_{factor}\left(\Delta\theta,\ \Delta\theta_{single}\right) = \frac{\sum_{n_c=1}^{N_c} CW_{n_c}(\Delta\theta)}{CW_{single}\left(\Delta\theta_{single}\right)}. \tag{48}$$

The $q_{factor}(\Delta\theta)$ describes the ratio between the capture width of a multi-chamber device with chambers having angular width $\Delta\theta$ and the capture width obtained from N_C independent single chamber devices with the same chamber width $\Delta\theta$. This parameter is used for evaluating the effects of the interferences due to the radiated waves that occur in a multi-chamber device, as it allows investigating whether the presence of additional chambers results in constructive or destructive interactions. The second one is the ratio between the capture width of a multi-chamber device with chambers having angular width $\Delta\theta$ against the capture width of a single chamber device spanning the full circle. The $r_{factor}\left(\Delta\theta,\ \Delta\theta_{single}\right)$ highlights the advantages and disadvantages of a multi-chamber device compared to the most common cylindrical OWC considered in literature.

3.1. Double chamber cylindrical OWC

The first numerical study concerns a vertical cylinder with two chambers having the same angular width $\Delta\theta_1 = \Delta\theta_2 = \pi$. The upwave chamber is located so that the bisector line is aligned with the incident wave direction. The performance of the system is evaluated via the non-dimensional parameters defined in Eq. (45) and the capture width in Eq. (43). The results are shown in frequency domain in Fig. 3. Note that, in order to emphasize the comparison against the single chamber case, Fig. 3 shows the results pertaining to the two chamber cases as well as the ones determined from a single chamber case. It is seen that the multi-chamber device exhibits larger output values into the upwave chamber, while there are no significant differences in the distribution over the frequency domain. Specifically, the volume excitation flow rate pertaining to the frontside chamber gains intensity and after the peak ($kd = 2.13$) decays as the single chamber OWC; the backside chamber has a slight shift of the flow rate peak towards lower frequencies ($kd = 2$) with a more rapid decay in the high frequency tail. Comparable conclusions can be drawn by comparing the radiation damping and the added mass of multi- and single-chamber OWC. The capture width plot shows that peaks are achieved at the same frequency values. The chamber exposed to the direct action of the incoming waves reaches higher values when embedded in a multi-chamber system.

The surface motion inside the chamber is strictly related to the examined frequency. In order to analyse the wave field inside the chamber, the first peak of the capture width has been taken into account ($kd = 2.13; \omega = 1.44$ rad/s). As shown in Fig. 4, the surface elevation has been plotted by considering both single and multi-chamber OWCs. As the incident wave field propagates, higher values are observed inside the chamber facing the incoming waves, especially near the inner vertical cylinder, while the back chamber shows surface levels below zero. Overall, it is seen that, given the same incident wave, the multi-chamber configuration gives rise to larger wave motion amplitudes, with a peak value close to $\eta_{max} = 1.6$, which is larger than the surface elevation peak value of $\eta_{max} = 1.2$ observed in the single chamber OWC.

3.2. Triple chamber cylindrical OWC

The second numerical study considers a vertical cylinder with three chambers having the same angular width $\Delta\theta_1 = \Delta\theta_2 = \Delta\theta_3 = 2\pi/3$. In this regard, note that chambers are numbered from the upwave one in anticlockwise order. Fig. 5 shows the results in terms of volume excitation flow rate, radiation damping, added mass and capture width, for the chamber 1 (continuous line), chamber 2 (dashed line), as well as for a single chamber OWC having the same angular width (dashed-dotted line). Due to the symmetry of chambers 2 and 3, the same numerical results are observed. Therefore, only one line is shown. An increase of volume excitation flow rate is seen in chamber 1 compared to the single OWC case. The peak is reached at the same frequency $kd = 2.16$, with a few differences in the low frequency band and an almost perfect overlap of the curves in the high frequency tail. The curve representing chamber 2 (and 3) shows a less marked trend, with a peak at a lower frequency

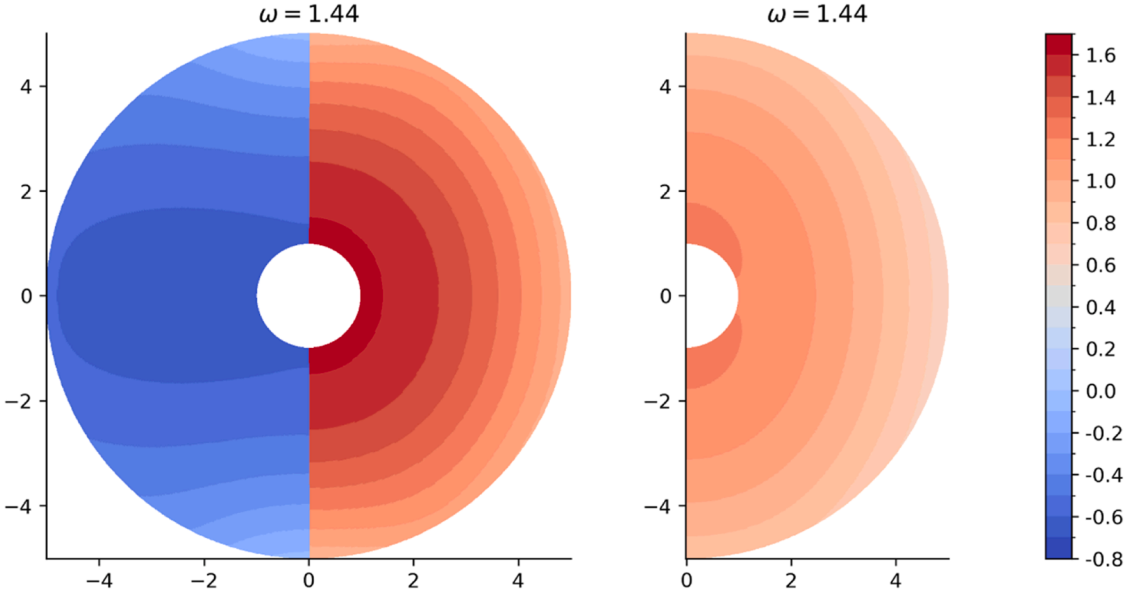

Fig. 4. Surface elevation inside the chamber (Left: multi-chamber OWC; Right: single chamber OWC). Top view.

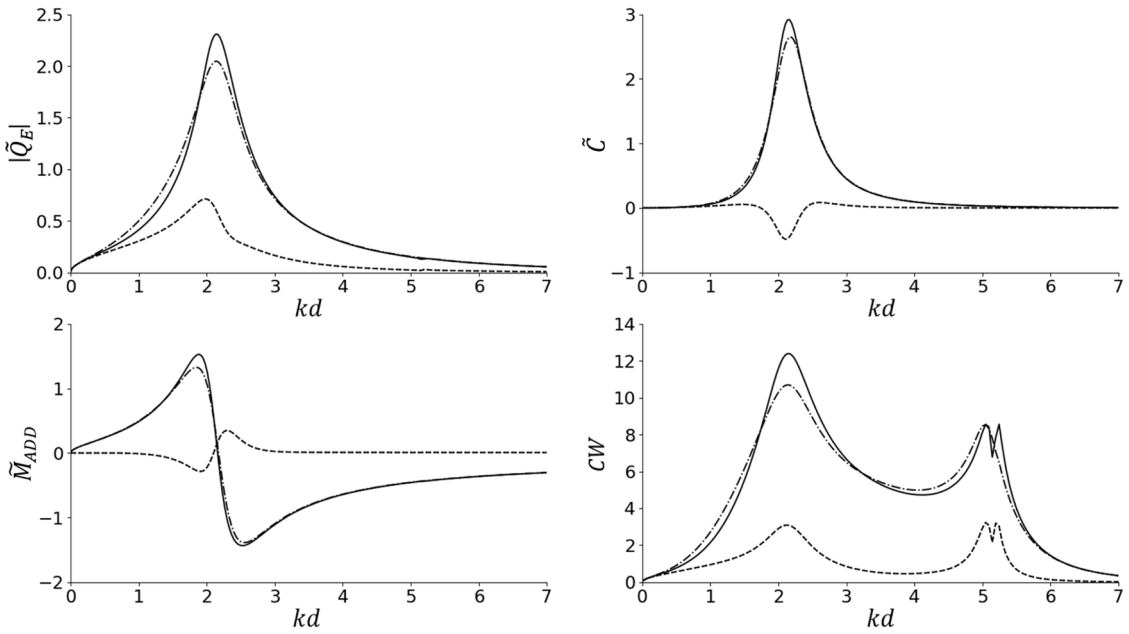

Fig. 5. Triple chamber OWC (Continuous line: upwave chamber; dashed line: both downwave chambers; dashed-dotted line: single upwave chamber).

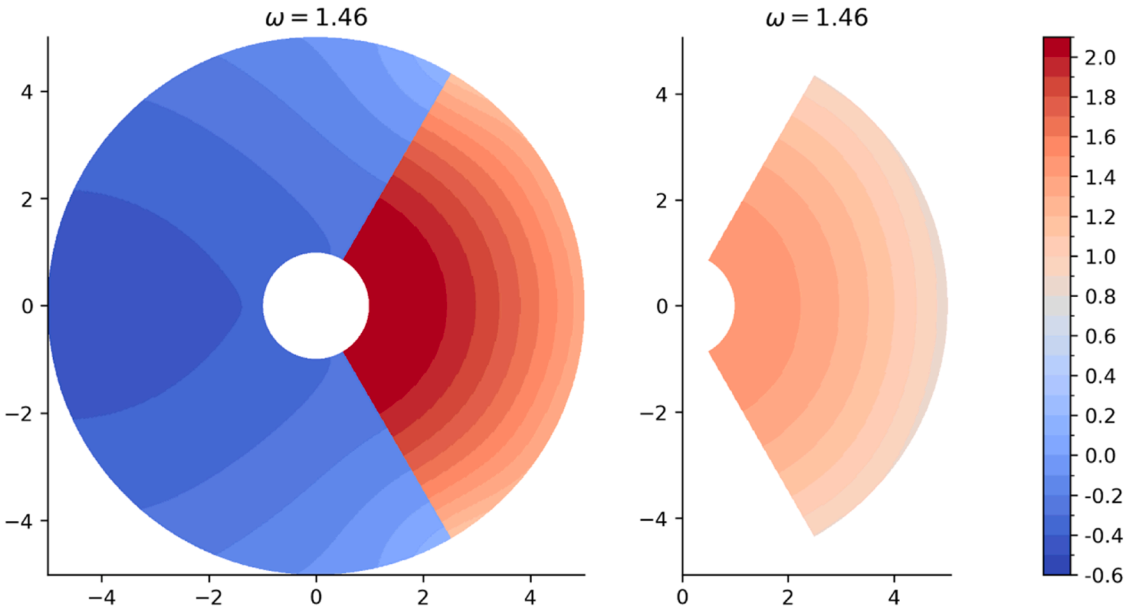

Fig. 6. Surface elevation inside the chamber (Left: multichamber OWC; Right: single chamber OWC). Top view.

($kd = 1.95$). The damping and added mass curves of the upwave chamber and of the single OWC chamber show quite similar patterns. The only difference relates to a more marked peak of chamber 1. Instead, chamber 2 exhibits significantly lower values of all the parameters under investigation, that can take also negative values as expected by the fact that are curves pertaining to the out-of-diagonal elements of the added mass and radiation damping matrices. The CW plot shows that the multi-chamber system offers advantages in terms of energy peaks, especially in the chamber exposed to the direct incident wave action.

For analysing the wave motion inside the chamber of the device, the frequency associated with the first peak of the CW is considered ($kd = 2.16; \omega = 1.46\ rad/s$). Fig. 6 shows a top view of the free surface displacement. It is seen that the use of a multi-chamber system amplifies the oscillation inside the chamber, with higher values ($\eta_{max} = 2$) near the cylinder's center compared to the single-chamber case ($\eta_{max} = 1.2$). Chambers 2 and 3 exhibit symmetrical behavior, with a negative free surface elevation value due to the phase difference with respect to the crest in chamber 1 and shallower troughs ($\eta_{min} = -0.6$).

3.3. Multi-chamber OWC vis-à-vis single-chamber OWC

Comparisons are pursued between single-chamber and multi-chamber devices via the $r_{factor}(\Delta\theta)$. As shown by Spanò et al. (2024), the parameter that most influences the energy production of a cylindrical OWC is the angular width of the chamber. Considering $\mathrm{CW}_{\mathrm{total}}$ as the sum of the CW reached by every chamber:

$$\mathrm{CW}_{\mathrm{total}} = \sum_{n_c=1}^{N_c} CW_{n_c}, \tag{49}$$

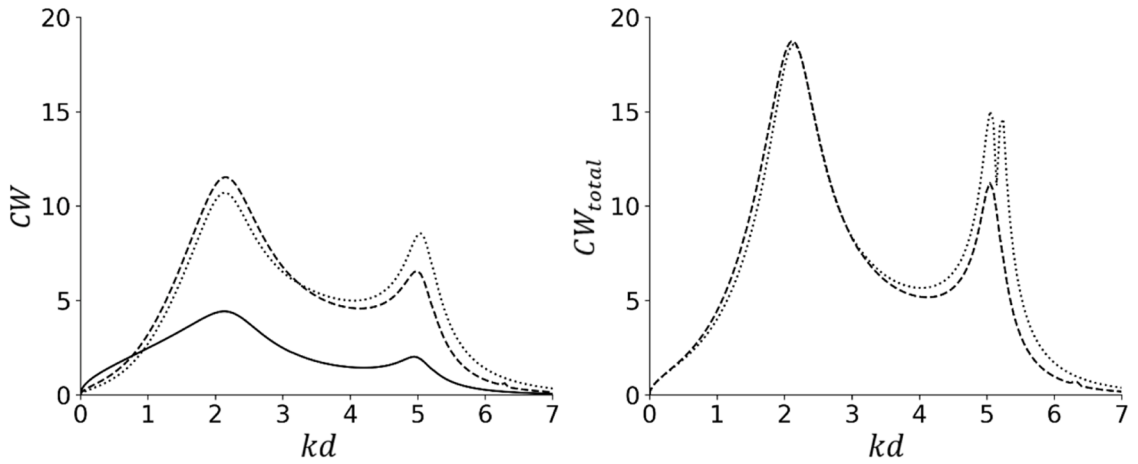

Fig. 7. CW_{total} of a single-chamber OWC (left) and multi-chamber OWC (right). (Continuous line: $\Delta\theta = 2\pi$; dashed line: $\Delta\theta = \pi$; dotted line: $\Delta\theta = 2\pi/3$).

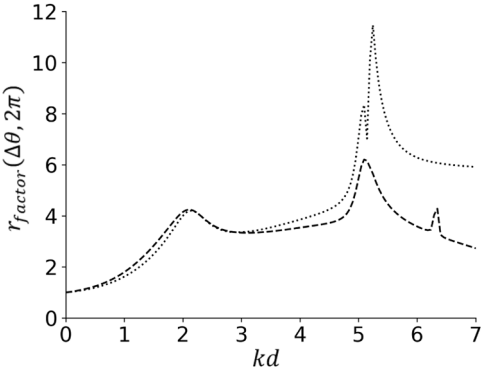

Fig. 8. r_{factor} concerning $\Delta\theta = \pi$ (Nc=2, dashed line) and $\Delta\theta = 2\pi/3$ (Nc=3, dotted line), against a single chamber OWC with $\Delta\theta_{single} = 2\pi$.

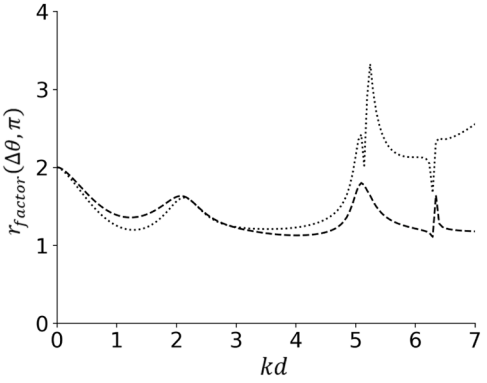

Fig. 9. . r_{factor} concerning $\Delta\theta = \pi$ (Nc=2, dashed line) and $\Delta\theta = 2\pi/3$ (Nc=3, dotted line), against a single chamber OWC with $\Delta\theta_{single} = \pi$.

Fig. 7 shows the CW values for single-chamber devices (left panel), with angular widths of $\Delta\theta = 2\pi$ (continuous line), $\Delta\theta = \pi$ (dashed line), and $\Delta\theta = 2\pi/3$ (dotted line). The right panel shows the CW_{total} for multi-chamber devices with $N_c = 2$ ($\Delta\theta_{nc} = \pi$, dashed line) and $N_c = 3$ ($\Delta\theta_{nc} = 2\pi/3$, dotted line) chambers. In case of single-chamber devices, reducing the internal angle significantly increases the CW peak. Furthermore, the reduction of the chamber angular width is associated with a more efficient exploitation of the high frequency waves. The right panel show that the CW_{total} of the two devices reaches even higher values.

The $r_{factor}(\Delta\theta,\ \Delta\theta_{single})$ has been introduced to evaluate the difference between a single OWC equipped with multiple chambers. Fig. 8 shows the $r_{factor}(\Delta\theta, 2\pi)$ with two lines, corresponding to the case of $N_c = 2$ ($\Delta\theta = \pi$, dashed line) and $N_c = 3$ ($\Delta\theta = 2\pi/3$, dotted line) against the CW_{total} pertaining to a single chamber OWC with $\Delta\theta = 2\pi$. The two lines follow a similar trend up to $kd = 3.09$, highlighting a significant increase in the productivity of multi-chamber devices compared to the more common single-chamber device found in the literature. Moving towards higher frequencies, the presence of more chambers allows harvesting more efficiently the available wave energy. Overall, this parameter highlights the convenience of splitting the OWC into multiple chambers to better harvest the wave energy in shorter waves.

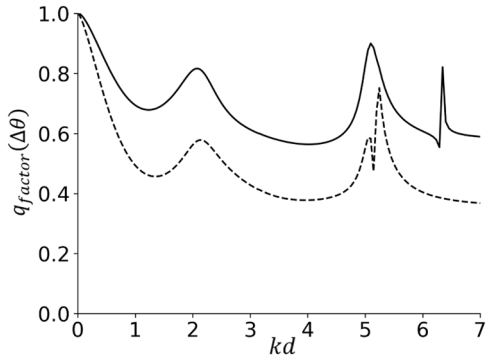

Fig. 10. $q_{factor}(\Delta\theta)$ (Continuous line: Nc=2; dashed line: Nc=3).

As depicted in Fig. 7, the optimal strategy to significantly increase the energy-wise performance of a cylindrical OWC is to reduce the angular width of the internal chamber, with $\Delta\theta = \pi$ being the optimal solution. To verify whether this solution remains advantageous compared to a multi-chamber device, the $r_{factor}(\Delta\theta,\ \pi)$ is calculated by comparing the CW of the two multi-chamber devices (Nc = 2 dashed line; Nc = 3 dotted line) to a single-chamber OWC with an angular width of $\Delta\theta_{single} = \pi$. From Fig. 9, it is shown how at low frequencies, where piston-like motion in the chamber is dominant, the productivity of the devices is doubled. The entire curve stays above 1, suggesting the further effectiveness of the multi-chamber system compared to the optimal solution of a single-chamber OWC with reduced angular width.

Next, the $q_{factor}(\Delta\theta)$ is taken into account. As shown in Fig. 10, $q_{factor}(\Delta\theta)$ is plotted for the cases of two-chamber devices (continuous line) and three-chamber devices (dashed line). At low frequencies, the curves show a similar behavior. Moving to higher frequencies, they show an almost constant difference of approximately 0.2. The first and second peak of the $q_{factor}(\Delta\theta)$ are observed at the associated CW peaks ($kd = 2.13$ for the $N_c = 2$ case, $kd = 2.16$ for the $N_c = 3$ case). The

minimum value reached by the curve representing the $N_c = 2$ case is around 0.6. This means that a device equipped with two chambers can potentially reach the 80–60 % CW values achieved by an array of two (non-interacting) devices equipped individually with just one chamber of equal size. For the $N_c = 3$ case, CW reaches a minimum of 0.39. In this case, a multi-chamber device equipped with three chambers can theoretically reach from 39 % to 78 % the CW values achieved by three independent OWCs equipped with one chamber of equal size.

4. Concluding remarks

Common studies conducted on cylindrical OWCs focus on devices comprising a single chamber spanning the entire inner space. To maximize energy production, research is moving towards devices with multiple chambers arranged concentrically. This study considers the arrangement of multiple chambers with reduced angular widths, whose performance is compared vis-à-vis the results of a classical single chamber OWC spanning the entire circular sector or just a limited angular width.

This paper presents an analytical solution based on the linearized potential flow theory. Diffracted and radiated wave fields have been determined by using the eigenfunction expansion matching method. A linear PTO has been considered. The analysis has concerned volume excitation flow rates, radiation damping, added mass and capture width values.

Two cases concerning a vertical cylinder equipped with two and three chambers, respectively, have been investigated. In both cases, the upwave chamber is oriented such that the bisector line is aligned along the upcoming incident wave direction. Both cases show an increase in capture width for multi-chamber devices, especially when compared to a single-chamber OWC device having the same angular width. This fact has been observed also by evaluating the surface elevation inside the chamber.

The $r_{factor}\left(\Delta\theta,\ \Delta\theta_{single}\right)$ was introduced to compare the advantage of a multi-chamber device compared to a single-chamber OWC. The results highlight the improvement of a multi-chamber OWC compared to the classical circular OWC with an angular width spanning the full sector $\Delta\theta = 2\pi$, and also against a single chamber characterized by $\Delta\theta = \pi$.

The $q_{factor}(\Delta\theta)$ was used for evaluating the interferences that occur between the chambers of a multi-chamber OWC. The results show a few reductions in terms of productivity.

This paper examined a multi-chamber OWC device by adopting a semi-analytical approach in the framework of the linear potential flow theory. Therefore, overestimations due to neglecting the effects of viscosity and the modelling of air compressibility may characterize the obtained numerical results. For this reason, future studies will consider other models, such as the ones based on Computational Fluid Dynamics, or experimental tests for assessing the performance of the system.

CRediT authorship contribution statement

Antonino Simone Spanò: Software, Formal analysis, Writing – original draft, Methodology, Conceptualization. **Giovanni Malara:** Writing – review & editing, Methodology, Supervision, Conceptualization. **Felice Arena:** Supervision, Writing – review & editing, Conceptualization.

Declaration of competing interest

The authors declare that they have no known competing financial interests or personal relationships that could have appeared to influence the work reported in this paper.

References

Abhinav, K.A., Collu, M., Benjamins, S., Cai, H., Hughes, A., Jiang, B., Jude, S., Leithead, W., Lin, C., Liu, H., Recalde-Camacho, L., Serpetti, N., Sun, K., Wilson, B., Yue, H., Zhou, B.Z., 2020. Offshore multi-purpose platforms for a blue Growth: a technological, environmental and socio-economic review. Sci. Total Environ. 734, 138256. https://doi.org/10.1016/J.SCITOTENV.2020.138256.

Abramowitz, M., Stegun, I., 1964. Handbook of mathematical functions: with formulas, graphs, and mathematical tables.

Babarit, A., 2015. A database of capture width ratio of wave energy converters. Renew. Energy 80, 610–628. https://doi.org/10.1016/j.renene.2015.02.049.

Joao, Cruz, 2008. Ocean wave energy: Current Status and Future Perspectives. Springer-Verlag Berlin Heidelberg. https://doi.org/10.1007/978-3-540-74895-3.

Deng, Z., Huang, Z., Law, A.W.K., 2014. Wave power extraction from a bottom-mounted oscillating water column converter with a V-shaped channel. Proceedings of the Royal Society A: Mathematical, Physical and Engineering Sciences 470. https://doi.org/10.1098/rspa.2014.0074.

Evans, D.V., Porter, R., 1995. Hydrodynamic characteristics of an oscillating water column device. Appl. Ocean Res. 17, 155–164. https://doi.org/10.1016/0141-1187(95)00008-9.

Falcão, A.F., de, O., 2010. Wave energy utilization: a review of the technologies. Renew. Sustain. Energy Rev. 14, 899–918. https://doi.org/10.1016/J.RSER.2009.11.003.

Falcão, A.F.O., Henriques, J.C.C., Gato, L.M.C., 2016. Air turbine optimization for a bottom-standing oscillating-water-column wave energy converter. J. Ocean Eng. Mar. Energy 2, 459–472. https://doi.org/10.1007/s40722-016-0045-7.

Fu, L., Wang, R., Ning, D., Mayon, R., 2023. Numerical investigation on the hydrodynamic performance of a land-based OWC system with multi-chamber modules. Appl. Ocean Res. 141. https://doi.org/10.1016/j.apor.2023.103801.

Gang, A., Guo, B., Hu, Z., Hu, R., 2022. Performance analysis of a coast – OWC wave energy converter integrated system. Appl. Energy 311, 118605. https://doi.org/10.1016/J.APENERGY.2022.118605.

Gray, R.M., 2006. Toeplitz and Circulant Matrices: a review. Found. Trends® Commun. Inf. Theory 2, 155–239. https://doi.org/10.1561/0100000006.

Lamas-Pardo, M., Iglesias, G., Carral, L., 2015. A review of very large Floating structures (VLFS) for coastal and offshore uses. Ocean Eng. 109, 677–690. https://doi.org/10.1016/J.OCEANENG.2015.09.012.

Lehmann, M., Karimpour, F., Goudey, C.A., Jacobson, P.T., Alam, M.R., 2017. Ocean wave energy in the United States: current status and future perspectives. Renew. Sustain. Energy Rev. https://doi.org/10.1016/j.rser.2016.11.101.

Linton, C.M., McIver, P., 2001. Handbook of mathematical techniques for wave/structure interactions. Chapman & Hall/CRC.

Liu, Z., Zhang, X., Ding, L., Han, Z., Ni, H., 2024. Hydrodynamic and energy-harvesting performances of a compact-array OWC device: an experimental study. Energy 310, 133209. https://doi.org/10.1016/J.ENERGY.2024.133209.

Lovas, S., Mei, C.C., Liu, Y., 2010. Oscillating water column at a coastal corner for wave power extraction. Appl. Ocean Res. 32, 267–283. https://doi.org/10.1016/j.apor.2010.06.004.

Martins-Rivas, H., Mei, C.C., 2009. Wave power extraction from an oscillating water column at the tip of a breakwater. J. Fluid Mech. 626, 395–414. https://doi.org/10.1017/S0022112009005990.

Michele, S., Renzi, E., Perez-Collazo, C., Greaves, D., Iglesias, G., 2019. Power extraction in regular and random waves from an OWC in hybrid wind-wave energy systems. Ocean Eng. 191. https://doi.org/10.1016/j.oceaneng.2019.106519.

IEA, 2021. Electricity information: overview, IEA, Paris, https://www.iea.org/reports/electricity-information-overview, Licence: CC BY 4.0.

Mørk, G., Barstow, S., Kabuth, A., Pontes, M.T., 2010. Assessing the global wave energy potential, in: Proceedings of the International Conference on Offshore Mechanics and Arctic Engineering - OMAE. pp. 447–454. https://doi.org/10.1115/OMAE2010-20473.

Ning, D., Fu, L., Zhou, Y., Mayon, R., Zhang, Y., 2024. Hydrodynamic performance of a land-based multi-chamber OWC wave energy capture system: an experimental study. Coast. Eng. 190, 104510. https://doi.org/10.1016/J.COASTALENG.2024.104510.

Ning, D., Zhou, Y., Zhang, C., 2018. Hydrodynamic modeling of a novel dual-chamber OWC wave energy converter. Appl. Ocean Res. 78, 180–191. https://doi.org/10.1016/j.apor.2018.06.016.

Qian, K., Chen, L., Zhou, Y., Ning, D., 2024. Hydrodynamics of an offshore multi-chamber OWC wave energy converter. Energy 304, 132239. https://doi.org/10.1016/J.ENERGY.2024.132239.

Shi, X., Liang, B., Li, S., Zhao, J., Wang, J., Wang, Z., 2024. Wave energy resource classification system for the China east adjacent seas based on multivariate clustering. Energy 299, 131454. https://doi.org/10.1016/J.ENERGY.2024.131454.

Spanò, A.S., Malara, G., Arena, F., 2024. Response of an oscillating water column spanning a circle sector and embedded in a circular platform. Ocean Eng. 309. https://doi.org/10.1016/j.oceaneng.2024.118389.

Taveira-Pinto, F., Iglesias, G., Rosa-Santos, P., Deng, Z.D., 2015. Preface to special topic: marine Renewable Energy. J. Renew. Sustain. Energy. https://doi.org/10.1063/1.4939086.

Zheng, S., Zhu, G., Simmonds, D., Greaves, D., Iglesias, G., 2020. Wave power extraction from a tubular structure integrated oscillating water column. Ren. Energy 150, 342–355. https://doi.org/10.1016/j.renene.2020.01.008.

Zhou, Y., Zhang, C., Ning, D., 2018. Hydrodynamic investigation of a concentric cylindrical OWC wave energy converter. Energies 11 (4), 985. https://doi.org/10.3390/en11040985.